Received: 15 April 2020 | Revised: 18 January 2021 | Accepted: 15 February 2021

DOI: 10.1049/cds2.12069

IET Circuits, Devices & Systems

The Institution of Engineering and Technology WILEY

ORIGINAL RESEARCH PAPER

Correlation between performance characteristics of indoor photovoltaic devices and DC-to-DC up-converters for low-power electronic applications

Khandaker A. Haque | **Md Zunaid Baten**

Department of Electrical and Electronic Engineering, Bangladesh University of Engineering and Technology, Dhaka, Bangladesh

Correspondence

Md Zunaid Baten, Department of Electrical and Electronic Engineering, Bangladesh University of Engineering and Technology, Dhaka 1205, Bangladesh.
Email: mdzunaid@eee.buet.ac.bd

Abstract

This study presents a numerical analysis to correlate performance characteristics of indoor photovoltaic (PV) devices with those of DC-to-DC up-converters designed for low-power electronic applications. A theoretical model based on self-consistent solution of Poisson's equation and continuity equation under optical generation-recombination conditions has been applied to design $Cu_2ZnSn(SSe)_4$-based PV devices having type-I and type-II energy band profiles, such that they can operate with peak efficiencies of 12.6% and 14.1%, respectively, under illumination from an experimentally characterized white light-emitting diode. Each PV device has been subsequently utilized as the input source of a Meissner oscillator-based self-driven DC-to-DC converter. Comparative analysis shows that in spite of the lower PV conversion efficiency, the PV device having higher short-circuit current density results in a higher output efficiency of the converter circuit. Similar characteristic trends are obtained for a boost converter operating in a discontinuous conduction mode, whereas a continuous conduction mode of operation results in the opposite trend. The underlying reason behind such an observation has been traced back to the transient behaviour of the inductor current of the converter. The results of this study suggest close correlation between physics-based design parameters of the PV device and output performance characteristics of the converter circuit.

1 | INTRODUCTION

The modern era has seen phenomenal advancements in the field of electronics, where the size of electronic devices has diminished significantly with the passage of time. Such advancements, accompanied by the incredible developments in the telecommunication sector, has made it possible for electronic devices coming from variegated sources to be cyber-connected such that they can form a complex network of 'things'—a paradigm popularly known as the Internet of Things (IoTs). The interconnected mesh of IoTs constitutes a cyber–physical system, which is considered to be the cornerstone of the ongoing fourth industrial revolution [1, 2]. The remarkable advancement of IoTs and cyber–physical systems has resulted in a surge in the demand for reliable, non-exhaustible sources of energy supply, so that the constituent low-power electronic devices can operate reliably for long hours irrespective offrequent or sudden power-cuts, and at the same time maintain the lowest possible, if not zero, carbon emission. Conventionally, batteries of different kinds are utilized to power-up wired or wireless communication nodes, sensors, actuators and other low-power components of cyber–physical systems. However, irrespective of the technology, batteries need to be replaced over time and at the end of their limited life cycles, they pose significant threat to the environment in the form of electronic waste.

To overcome the shortcomings of conventional exhaustible sources of energy supply, efficient utilization of renewable energy resources is being considered as the most viable way forward. Energy harvesting by means of the photovoltaic (PV) energy conversion [3], thermoelectric generation [4] or motion sensing [5] is gaining a significant interest in this regard. Energy scavenging employing PV devices in particular has gained much prominence because of the higher efficiency and

reliability of these devices compared to other sources, such as the piezoelectric vibrators or thermoelectric generators [6–10]. Thin-film PV devices designed and realized with different material systems, such as CIS, CIGS [11], GaAs, GaInP [12, 13], CdTe [14], peroskvites [15] etc., have been reported to show promising characteristics in this regard. However, from a practical point of view, it is important to note that irrespective of the material system, output voltage of a single PV device is not high enough to drive a regular electronic device or an entire sensor node. So, energy harvesting only with a single PV device, no matter how attractive it sounds, will fail to meet the practical needs unless supplementary means are incorporated.

Utilization of power electronic driver circuits—comprising of BJTs, FETs or SCRs—appears to be the most logical approach towards fulfilling the requirements of low-power electronic loads, while being powered up by indoor PV devices. Though significant efforts have been invested on designing and developing indoor PV devices, it remains to be seen how solid-state physics-based design parameters of these devices are going to influence design considerations of DC-to-DC up-converter circuits to be used for driving low-power electronic devices. This necessitates the need for device-circuit co-design, which is already an active domain of research in the study of novel materials and devices for next generation computing, neuromorphic and power-electronic applications [16–19]. Though such an approach has not been adopted in the field of indoor PVs, it is envisaged that there is significant scope of exploring the prospect of co-designing PV devices and the corresponding DC-to-DC up-converter circuits such that the requirements of low-power electronic loads are best served when the PV device is used in conjunction with its co-optimized driver circuit or vice versa. This study aims to investigate this untapped area of research in the overlapping fields of indoor PVs and low-power electronics, which altogether promises to be a highly prospective area of exploration in the burgeoning field of micro-energy harvesting for loTs and cyber–physical systems.

Here, physics-based design parameters of an indoor solid-state lamp operated PV device are correlated with performance characteristics of DC-to-DC up-converters operated in tandem with the PV device for driving low-power electronic components of IoTs. As the PV energy converter, we consider here a $Cu_2ZnSn(SSe)_4$- or CZTSSe-based PV device, which recently has been proposed as a low-cost, energy-efficient solution for indoor PV applications [20]. As for the power electronic driver, both conventional boost converters and a self-driven DC-to-DC converter based on the concept of the Meisnner oscillator have been considered. PV devices having type-I and type-II energy band profiles are respectively taken as inputs to the converter circuits and the corresponding performance characteristics of the converters have been evaluated based on numerical analysis. The results of this analysis suggest that output efficiency of the converter circuit can be enhanced by increasing the short-circuit current density of the PV device, even if it might degrade PV conversion efficiency of the latter. The underlying reason has been explained based on the discontinuous conduction mode of operation of the conventional boost converter, and also on the basis of transient characteristics of the converter circuits. The overall results of this study suggest that performance characteristics of power-electronic converter circuits are strongly dependent on the physics-based design parameters of the PV device being used as the input source. This study thereby establishes a link between two different, yet closely related, areas of research related to the PV energy conversion technology, namely the solid-state device physics and power-electronics.

2 | NUMERICAL ANALYSIS OF PV SOURCES

Two CZTSSe-based PV devices having slightly different heterostructures have been considered as PV sources for driving low-power electronic loads in this study. Schematic diagrams detailing heterostructures of these devices, labelled as Device A and Device B respectively, are shown in Figure 1(a) and (b). As can be observed, both these devices comprise of the p-type CZTSSe absorber layer, the n-type CdS buffer layer and the n-type transparent conducting oxide layer. In Device A, ITO is placed on top of the n-type ZnO layer to form the n-contact, whereas in Device B an Al-doped ZnO residing over intrinsic ZnO buffer layer is used as the n-contact. Such choice of buffer layer causes the energy band diagram of Device A to be of straddling type, that is, of type-I in nature (Figure 1(c)). On the other hand, the energy band diagram of Device B is staggered (type-II) in nature, as has been shown in Figure 1(d). The performance characteristics of these devices have been evaluated considering irradiation by a commercially available 15W, 497 lumen white LED. The experimentally measured spectra of this LED, which is characterized to have a colour rendering index (CRI) of 75.74% and correlated colour temperature (CCT) of 6175 K, is shown in Figure 2(a).

To evaluate the performance characteristics of both Devices A and B under the considered indoor illuminating spectra, a theoretical model based on the numerical solution of the Poisson's equation and the continuity equation under optical generation-recombination conditions is considered [20]. Considering z-axis to be the direction of light propagation and carrier transport through the device (Figure 1(a) and (b)), the following 1-D Poisson's equation is numerically solved, taking into account the relevant boundary conditions at the hetero-interfaces and at the top and bottom contacts of the device:

$$\frac{\varepsilon_r(z)}{q}\frac{\partial^2\varphi(z)}{\partial z^2} = p(z) - n(z) + N_D(z) - N_A(z) \qquad (1)$$

Here $\varepsilon_r(z)$ is the dielectric permittivity of the medium, q is the electron charge, $N_A(z)$ and $N_D(z)$ are the acceptor and donor concentrations, and $n(z)$, $p(z)$ are the free electron and hole densities, respectively. Upon solving Poisson's equations, the following continuity equations and drift-diffusion equations are solved iteratively in a coupled manner to obtain the

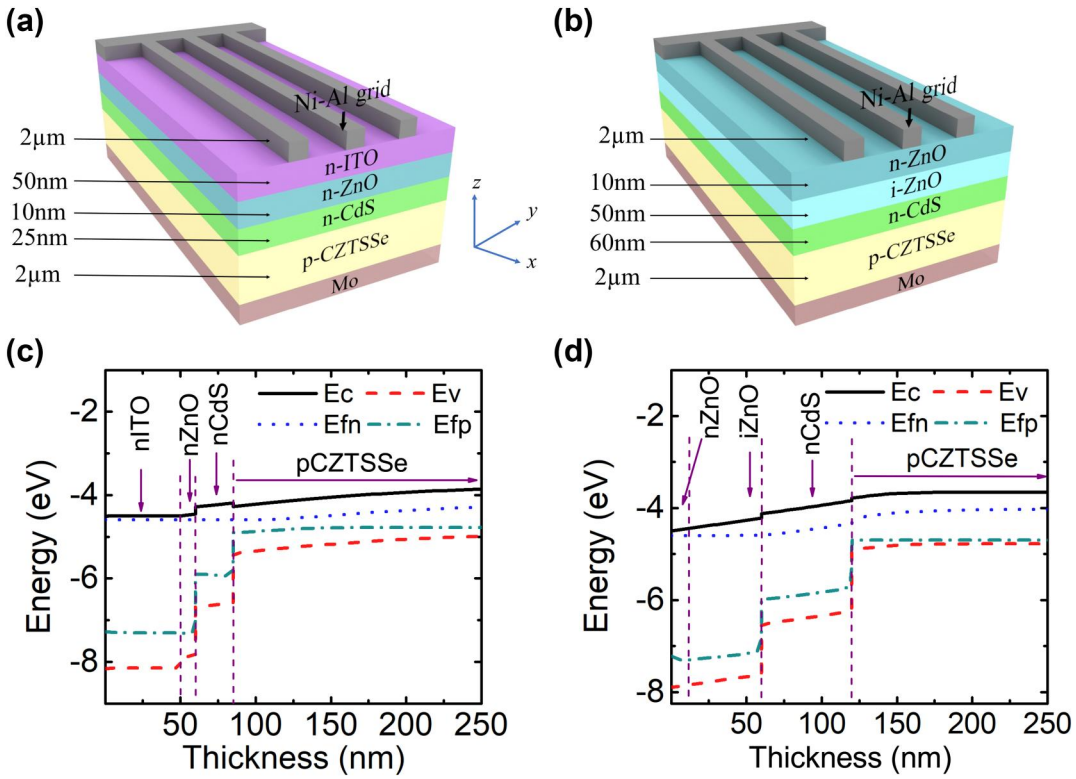

FIGURE 1 Schematic illustration of heterostructures of (a) Device A and (b) Device B; non-equilibrium energy band diagrams of (c) Device A and (d) Device B

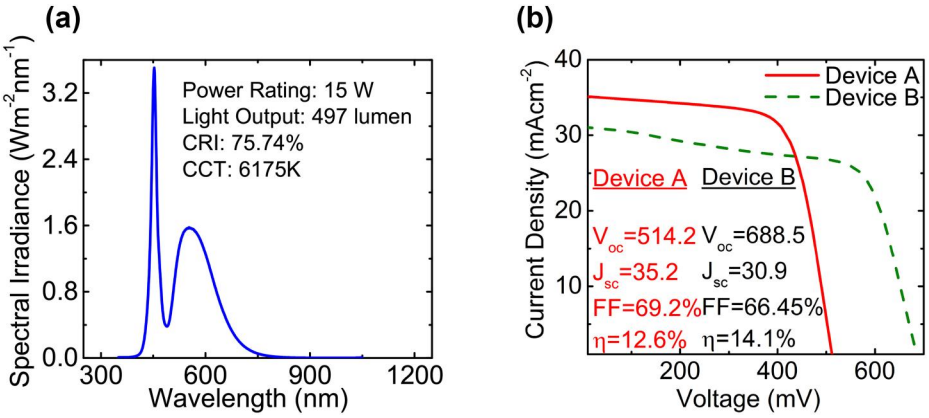

FIGURE 2 (a) Measured white LED spectrum; (b) simulated J–V characteristics of Device A and Device B under 1000 Wm^{-2} irradiation of the white LED

electron and hole current densities, which are denoted as J_n and J_p, respectively.

$$J_n = q\mu_n n(z)\frac{\partial}{\partial z}E_{Fn}(z) \tag{2}$$

$$J_p = q\mu_p p(z)\frac{\partial}{\partial z}E_{Fp}(z) \tag{3}$$

$$-\frac{1}{q}\frac{\partial J_n}{\partial_z} = G_n(z) - R_n(z) \tag{4}$$

$$+\frac{1}{q}\frac{\partial J_p}{\partial_z} = G_p(z) - R_p(z) \tag{5}$$

Here, E_{F_n} and E_{F_p} are the electron and hole quasi-Fermi levels, which are estimated from the Boltzmann approximation of the Fermi–Dirac distribution function. The electron (μ_n) and hole (μ_p) mobility values, along with other material parameters used in this study, are shown in Table 1. These values have been taken from previous works reported in [21–35]. The electron (hole) recombination rates R_n (R_p)

TABLE 1 List of material parameters used for Device A (Device B)

Parameters	n-ITO (n-ZnO)	n-ZnO (I-ZnO)	n-CdS (n-CdS)	*p*-CZTSSe (*p*-CZTSSe)
Layer thickness (cm)	5×10^{-6} (1×10^{-6})	1×10^{-6} (5×10^{-6})	2.5×10^{-6} (6×10^{-6})	2×10^{-4} (2×10^{-4})
Mobility gap (eV)	3.65 (3.4)	3.4 (3.4)	2.4 (2.4)	1.13 (1.13)
Optical gap (eV)	3.65 (3.4)	3.4 (3.4)	2.4 (2.4)	1.13 (1.13)
Donor doping (cm^{-3})	7×10^{19} (2.2×10^{16})	1×10^{16} (0)	1.5×10^{16} (1.1×10^{16})	0 (0)
Acceptor doping (cm^{-3})	0 (0)	0 (0)	0 (0)	1×10^{16} (7×10^{16})
Dielectric constant	5.2 (7.96)	7.96 (7.96)	10 (10)	10 (10)
Electronic affinity (eV)	4.515 (4.5)	4.515 (4.5)	4.34 (4.4)	4.422 (4.422)
Effective density of states (DOS) in CB (cm^{-3})	3×10^{21} (3.92×10^{18})	3.92×10^{18} (3.92×10^{18})	2.22×10^{18} (2.22×10^{18})	4.22×10^{18} (4.22×10^{18})
Effective density of states (DOS) in VB (cm^{-3})	2×10^{21} (3.34×10^{18})	3.34×10^{18} (3.34×10^{18})	1.8×10^{21} (1.8×10^{21})	4.2×10^{18} (4.2×10^{18})
Electron mobility ($cm^2V^{-1}s^{-1}$)	75 (40)	40 (40)	340 (340)	40 (40)
Hole mobility ($cm^2V^{-1}s^{-1}$)	40 (3)	3 (3)	40 (40)	10 (10)
Band to band recombination Coefficient (cm^3s^{-1})	5×10^{-07} (5×10^{-07})	5×10^{-06} (5×10^{-06})	9×10^{-08} (9×10^{-08})	1×10^{-09} (1×10^{-09})

Abbreviations: CB, conduction band; VB, valence band.

appearing in Equations (4) and (5) are calculated using the following relation considering band-to-band recombination under the steady state condition.

$$R(z) = r^{BB}\left\{n(z)p(z) - N_C N_V e^{-E_g(z)/kT}\right\} \quad (6)$$

Here $E_g(z)$ is the material band gap, k is the Boltzmann constant, T is the operating temperature, $N_C(z)$ and $N_V(z)$ are effective density of states of the conduction and valence bands respectively, and r^{BB} is the band-to-band recombination coefficient of the corresponding layer. To incorporate the effect of indoor illumination, electron (hole) generation rates, denoted as G_n (G_p) in Equations (4) and (5), are calculated using the following relation:

$$G(z) = \int d\lambda \phi_0(\lambda) R(\lambda) A(\lambda) \alpha(\lambda) e^{-\alpha(\lambda)z} \quad (7)$$

Here λ is wavelength of the incident light, $\alpha(\lambda)$ is the absorption coefficient of the material and $\phi_0(\lambda)$ is the incident photon flux. Spectrally resolved reflectance ($R(\lambda)$) and absorptance ($A(\lambda)$) resulting from coherent or incoherent internal multiple reflections are calculated considering complex refractive index and total internal reflection in the semiconductor stack. It is to be noted that the numerical model described here is first validated with experimental results reported for the highest efficiency CZTSSe solar-cell [32].

Current density versus voltage ($J - V$) characteristics of both Devices A and B, calculated using the numerical model, are shown on the same plot in Figure 2(b) along with their figure of merits. As can be observed, under identical illumination conditions, Device A has a higher short circuit current density (J_{sc}) than does Device B However, the open circuit voltage (V_{oc}) of Device A is lower than that of Device B by about 0.17 V, which ultimately results in the higher efficiency of Device B The larger V_{oc} of Device B arises from its specific nature of the energy band profile, which results in a relatively higher built-in field of about 6.6×10^8 V/cm at the junction. This is further evident from the non-equilibrium energy band diagrams shown in Figure 1(c) and (b), which clearly exhibit larger splitting between quasi Fermi levels in Device B than in Device A. Even though the relatively low electron and hole mobilities of intrinsic ZnO layer results in lower fill-factor (FF) of Device B, the enhancement of V_{oc} more than compensates for this shortcoming, ultimately resulting in about 1.5% higher peak efficiency of Device B than that of Device A The two devices considered herein therefore represent two variants of a PV device having identical absorber material and slightly different conversion efficiencies. However, because of the differences in their energy band alignments, Device A attains its output efficiency primarily by a dint of high J_s and Device B attains so by means of a relatively high V_{oc}. From the viewpoint of device–circuit co-design, it is important to understand how such opposing attributes of the PV device having relatively close conversion efficiencies can influence output performances, and therefore design considerations of the DC-to-DC converter to be used for driving low-power electronic loads.

3 | CORRELATION WITH DC-TO-DC CONVERTER PERFORMANCE

A self-oscillating power-electronic circuit, shown in Figure 3 (a), is considered as the DC-to-DC up-converter to drive low-power electronic appliances designed based on energy harvested by the indoor-PV devices. The converter circuit is based on the topology of Meissner oscillator and has been reportedly used earlier for power-electronic applications [36–38]. Self-starting DC-to-DC converters of similar topology have been reportedly used earlier for low-power electronic applications based on thermoelectric generators [37, 38]. This study has explored design considerations of this converter while being utilized in conjunction with indoor-PV devices. For comparison and analysis purpose, a conventional DC-to-DC boost converter is also considered (Figure 3(b)). As can be observed, an additional driving circuit is required for switching the transistor element of the boost converter, whereas the oscillator-based circuit is self-driven and does not require any external circuitry to drive its switching element, namely the junction-gate field-effect transistor (JFET). The JFET shown in Figure 3(a) is connected in series with the secondary coil (L_2) of a transformer having alternate polarity. During startup, the current through the primary coil (L_1) increases and causes the JFET to conduct. At the same time, voltage of opposite polarity builds up in the secondary winding such that the JFET becomes pinched off at one point and stops conducting. The opposite voltage is dissipated by the Meissner oscillator formed with the parallel combination of a capacitor (C) and an inductor (L). The values of L and C determine both the switching frequency and duty cycle of the JFET, which in this case are 1 kHz and 85.71%, respectively. Values of other circuit elements of the oscillator-based converter and also of the conventional boost converter are chosen such that the output voltage and the efficiency of the driver circuits are optimized.

As has been shown in Figure 3(a) and (b), the CZTSSe-based PV devices considered here are taken as inputs to both the self-driven converter and boost converter circuits. The equivalent circuit diagram of the PV devices is shown in Figure 3(c). To estimate the short circuit current (I_{sc}) and dark current (I_{dark}) of the equivalent circuit model, the cross-sectional area of both Devices A and B is taken as 1 cm^2. This area results in peak output power density of 12−14.5 Wm^{-2}, which should be enough to drive micro- or milli-Watt rated power electronic devices and sensor nodes. To obtain I_{dark}, dark current density (J_{dark}) of each PV device is calculated using the relation:

$$V_{oc} = \frac{kT}{q}\ln\left(\frac{J_{sc}}{J_{dark}} + 1\right) \tag{8}$$

where k is the Boltzmann constant, T is the absolute temperature, q is the electronic charge, and V_{oc} and J_{sc} are the respective open circuit voltage and short circuit current density of the devices obtained from the numerical analysis described in Section 2. Though the J–V characteristics of Figure 2(b) suggest that the series (R_s) and shunt (R_{sh}) resistance values of

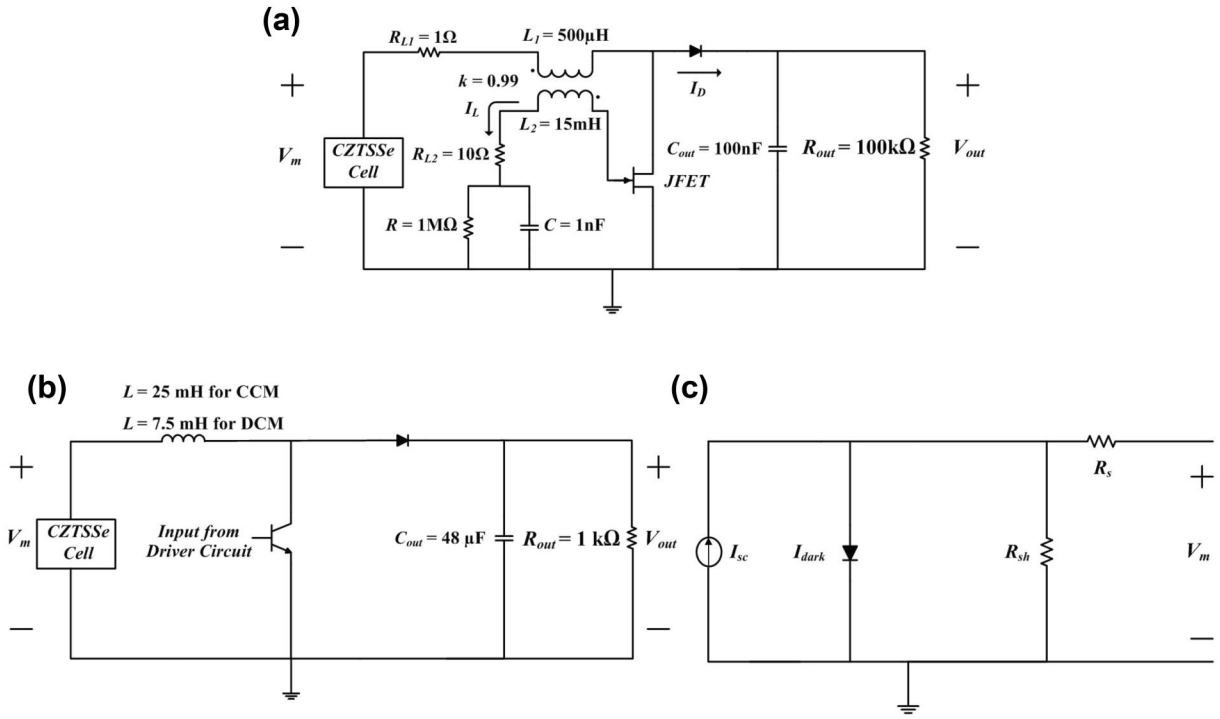

FIGURE 3 Circuit diagrams of (a) Meissner oscillator-based self-driven converter and (b) conventional boost converter having CZTSSe indoor device as the input source; (c) equivalent circuit diagram of the photovoltaic device

Devices A and B are unequal, the present study intentionally excludes the effect of series and shunt resistance variation on driver circuit performances. For this reason, fixed series and shunt resistance values of $R_s = 0.72\ \Omega cm^2$ and $R_{sh} = 621\ \Omega cm^2$, which are equal to the values reported for the highest efficiency CZTSSe solar cell [32], have been used in this study. Such consideration of identical R_{sh} and R_s for Devices A and B ensures that characteristic traits of the converter circuits will primarily be governed by the short circuit current density and open circuit voltage of the PV device being used as the input source.

To evaluate the output performance characteristics of the oscillator converter circuit of Figure 3(a), its output voltage (V_{out}) is simulated and plotted as a function of V_{oc} while keeping the J_{sc} values of the PV devices constant (Figure 4 (a)). On the other hand, in Figure 4(b), the dependence of V_{out} on J_{sc} is shown while keeping V_{oc} fixed at the characteristic values of Devices A and B It is to be noted that the red and blue circles in these plots and also in subsequent plots denote the actual operating points of Devices A and B, respectively. As can be observed from Figure 4, the output voltage of the converter is positively correlated with both J_{sc} and V_{oc}. Consequently, even though Device B has a smaller J_{sc} than does Device A, the former's higher value of V_{oc} ultimately results in a V_{out} comparable to what is obtained with Device A being used as the input source. Similar characteristics are observed in Figure 4(b), where, in spite of having a smaller V_{oc}, the higher J_{sc} value of Device A ultimately results in the converter circuit to give similar output voltages when Device A or B are used as the input sources. To understand how efficiency of the DC-to-DC converter (η_{os}) depends on V_{oc} and J_{sc} of the PV devices, η_{os} is calculated as a function of V_{oc} and J_{sc} while keeping corresponding J_{sc} and V_{oc} values constant. The results shown in Figure 4(c) and (d) suggest that converter efficiency is expected to increase with J_{sc}, whereas increasing V_{oc} has less of an effect on η_{os}. Consequently, the η_{os} value obtained while Device A is being used as the input source is about 1.2% higher than what is attained with Device B as the input.

To better understand the numerical results shown in Figure 4, semi-analytical expression of the output voltage V_{out} is derived based on the formalism and assumptions described in [39] for DC-to-DC converter operating in DCM. In this derivation, the series resistance of the inductor and the capacitor, as well as ON-resistance of the diode and JFET are ignored. In addition, for simplification of derivation, an equivalent inductance (L_{eq}) of the transformer is considered. Based on these considerations, when the JFET is OFF, the diode current (I_D) is given by:

$$I_D = \frac{V_{out}}{R_{out}} \tag{9}$$

Under this condition, I_D is related to the maximum inductor current (I_{max}) according to the following relation:

$$I_D \approx \left(\frac{1}{2} I_{max} D_1\right)\left(\frac{R}{R + R_{out}}\right) \tag{10}$$

$$where \quad I_{max} = \frac{V_m D_2}{L_{eq} f} \tag{11}$$

Here D_1 and D_2 are the duty cycles corresponding to decreasing and increasing inductor currents respectively, f is the frequency of operation, R and R_{out} are the resistance values shown in the circuit Figure 3(a). The term V_m is the output voltage of the PV device at its maximum power point. Comparing Equations (9), (10) and (11), we obtain:

$$D_2 = \frac{2 V_{out} L_{eq} f}{V_m D_1 R_{out}}\left(1 + \frac{R_{out}}{R}\right) \tag{12}$$

Under the DCM operation, the input and output voltages of the DC-to-DC converter are related by the following expression:

$$\frac{V_o}{V_m} = 1 + \frac{D_2}{D_1} \tag{13}$$

Therefore, comparing Equations (12) and (13), the following dependence of converter output voltage on PV device output is obtained:

$$V_{out} = \frac{1}{2}\left(1 + \sqrt{\frac{1 + 2D_2^2 R_{out}}{L_{eq} f}\left(\frac{R}{R + R_{out}}\right)}\right) V_m \tag{14}$$

It is to be noted that V_m is related to the PV device's open circuit voltage, short-circuit current and fill factor, which are all obtained from the numerical simulations described in Section 2. As can be observed from Figure 4, good agreement exists between numerical simulations and results obtained from the semi-analytical model described herein. It is obvious that the DC-to-DC converter output voltage and efficiency values are slightly overestimated if the series resistance and ON resistance of the inductor, capacitor, JFET and diode are ignored. Nevertheless, the results obtained from the simplified analytical model is found to be within ~5% of the numerical calculations. Both the analytical model and numerical simulation results suggest that even though the PV device with higher open circuit voltage (appearing from type-II energy band diagram of the device heterostructure) results in a higher output voltage of the self-oscillating DC-to-DC converter operating in DCM, the higher short-circuit current density of the device having type-I energy band diagram ultimately results in a higher converter efficiency. This calls for careful consideration during device-circuit co-design, for low-power applications of indoor PV devices.

It is obvious that the numerical and analytical results described in Figure 4(a) are specific to the DCM operation of the DC-to-DC converter, which is the mode under which the

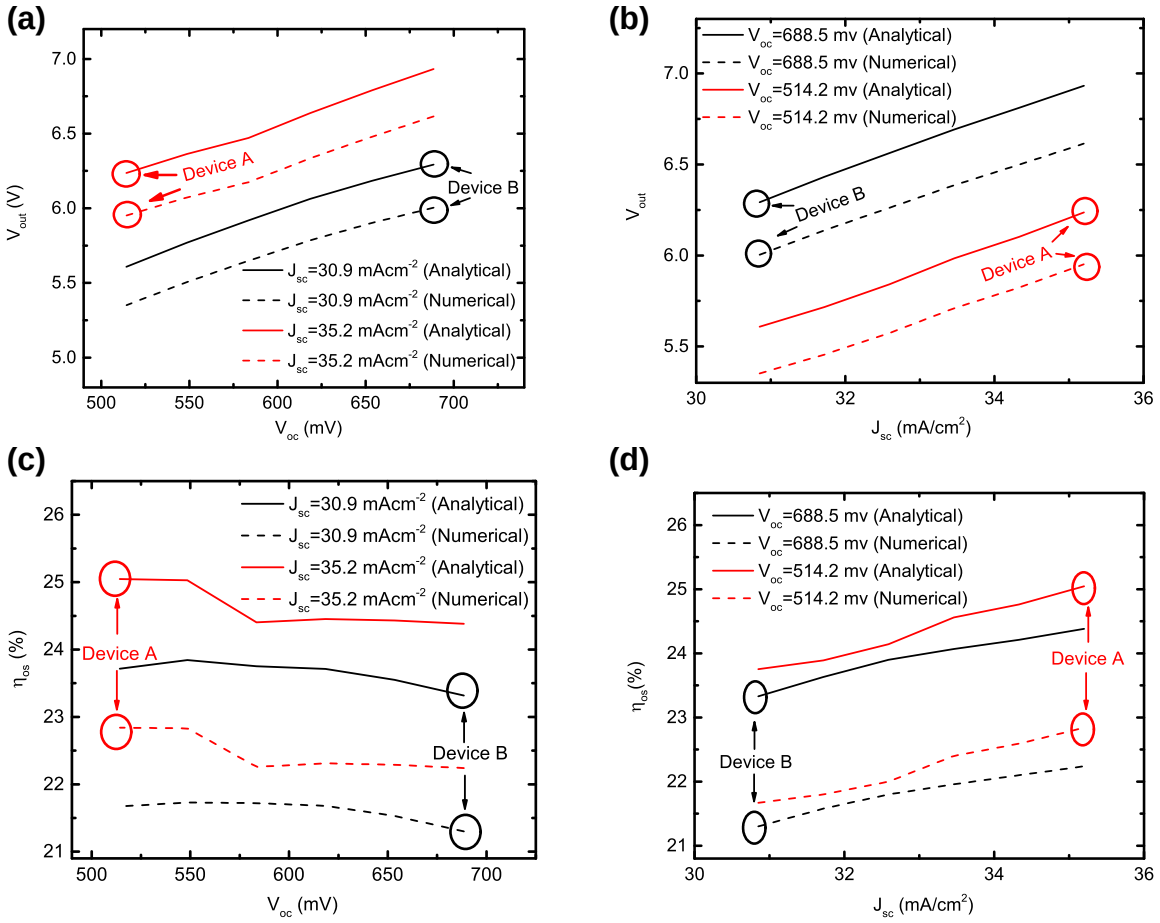

FIGURE 4 Output voltage of the self-driven converter obtained from numerical analysis and analytical expressions plotted as a function of (a) V_{oc} and (b) J_{sc}; output efficiency of the self-driven converter obtained from numerical analysis and analytical expressions plotted as a function of (c) V_{oc} and (d) J_{sc}, while other parameters of Devices A and B are kept constant

self-oscillating converter circuit of Figure 3(a) invariably operates. To better understand the influence of the mode of operation on the overall output performances of the PV device connected DC-to-DC converter, this study evaluates the performance characteristics of the conventional boost converter (shown in Figure 3(b)) while it is operated in both continuous and discontinuous conduction modes [40]. These modes of operations are determined by the inductance (L) of the boost-converter circuit such that for DCM of operation, L is lower than a minimum inductance (L_{min}). Here L_{min} is defined as:

$$L_{\min} = \frac{D(1-D)^2 R}{2f} \tag{15}$$

where D and f are duty cycle and frequency of operation of the converter circuit, respectively. Based on this calculation, inductance values of 7.5 and 25 mH have been utilized for DCM and CCM operations, respectively. As an oscillator-based converter invariably operates in DCM, for comparison purpose, the DCM-operated boost converter is designed such that it has duty cycle and frequency identical to that of the oscillator-based converter.

Output voltage of the boost converter operated in both CCM and DCM are shown in Figure 5(a) and (b) as a function of V_{oc} and J_{sc}, respectively, while keeping J_{sc} and V_{oc} constant. As can be observed, during the CCM operation, the device having a higher V_{oc} (i.e. Device B) results in a higher V_{out}. However, if the converter is designed to operate in DCM, the V_{oc} has less of an effect on V_{out}; as a result, the output voltages obtained for Devices A and B are essentially the same. Similar characteristic trends are observed from the η_{boost} versus V_{oc} and η_{boost} versus J_{sc} relations shown in Figure 5(c)–(d), where η_{boost} is output efficiency of the boost converter. While in the CCM, the converter efficiencies obtained for Devices A and B remain comparable. However, similar to the case of oscillator-based converter, during DCM operation, η_{boost} tends to increase with J_{sc} and it remains only weakly dependent on V_{oc}. Consequently, in DCM, the boost converter operates with about 1.5% higher efficiency when the device having higher J_{sc} (i.e. Device A) is used as the input source, even though the PV energy conversion efficiency of Device B is about 1.5% higher than that of Device A. Therefore, the results shown here suggest that output performance of the conventional boost converter operating in DCM closely resembles output characteristics of the oscillator-based converter.

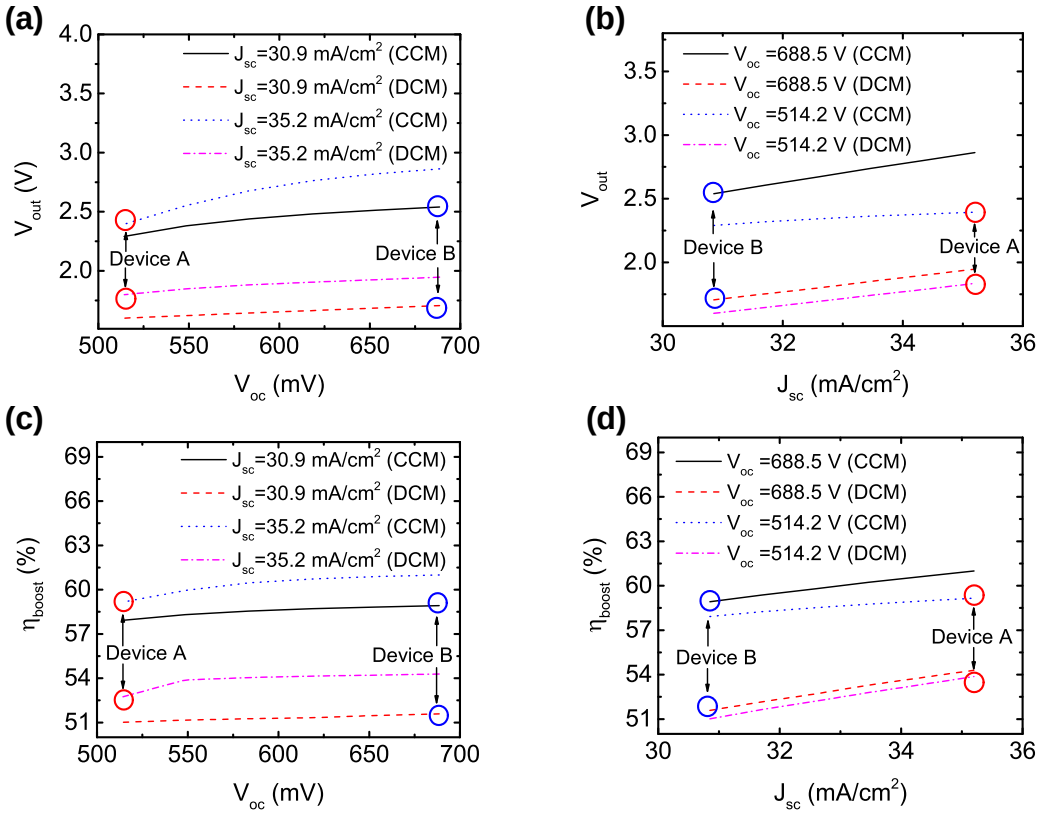

FIGURE 5 Output voltage of continuous conduction mode (CCM) and discontinuous conduction mode (DCM) operated boost converters plotted as a function of (a) V_{oc} and (b) J_{sc}, and conversion efficiency of CCM and DCM operated boost converters plotted as a function of (c) V_{oc} and (d) J_{sc} while other parameters of Devices A and B are kept constant

To gain further insight into the observed output characteristics, the transient response of the inductor current during the CCM and DCM operations of the conventional boost converter is simulated over several time cycles (Figure 6 (a)–(b)). As can be observed, during the CCM operation (Figure 6(a)), the inductor current (I_L) always remains positive irrespective of whether Device A or B is used as the input source. This ensures that the diode appearing in the boost converter circuit remains conducting and there is build-up of voltage at the output. On the contrary, during the DCM operation, the inductor current becomes negative over several cycles (Figure 6(b)), causing the diode to impede the flow of current to the external load. The alternate conduction paths under such circumstances are the diode and parasitic shunt resistance appearing in the equivalent circuit model of the PV device. Consequently, both voltage build-up and efficiency of the CCM operated boost converter appear to be higher than those of the DCM operated one. It is noteworthy that the current I_L tends to be less negative when Device A is used as the input source. This ultimately results in the higher conversion efficiency of the circuit when Device A is used as the input source, compared to the case when Device B is used as the input. Similar characteristic trends are observed from the transient response of the secondary inductor coil L_2 (Figure 3(a)) of the oscillator based converter circuit as well.

As has been shown in Figure 6(c), the inductor current I_L becomes negative irrespective of Device A or B being used as the input source. However, similar to the case of the DCM operated boost converter, the current I_L tends to decrease when Device B is used as the input instead of Device A. This trend is related to the characteristic resistance values of the PV devices, which are evaluated to be 13 and 21 Ω at the maximum power points of Devices A and B, respectively. However, the rise and fall time, as well as the time period and duty cycle of the transients are governed by elements of the DC-to-DC converter circuit, while the amplitude of the inductor current is observed to be significantly influenced by the characteristic resistance values of the PV devices. To further illustrate this aspect, inductor current of the self-oscillator based converter is calculated and plotted for different characteristic resistances of a PV device being used as the input source (Figure 6(d)). As can be observed, a higher characteristic resistance of the PV device results in a smaller inductor current of the converter circuit. This is in accordance with the results shown in Figure 6(c), where the lower characteristics resistance of Device A results in a larger inductor current I_L. Therefore, the intrinsic characteristics of Device A ultimately results in a higher output efficiency of the oscillator-based converter when it is used as the PV input source. Even though, Device B has a higher efficiency and open circuit voltage than does Device A, the former's

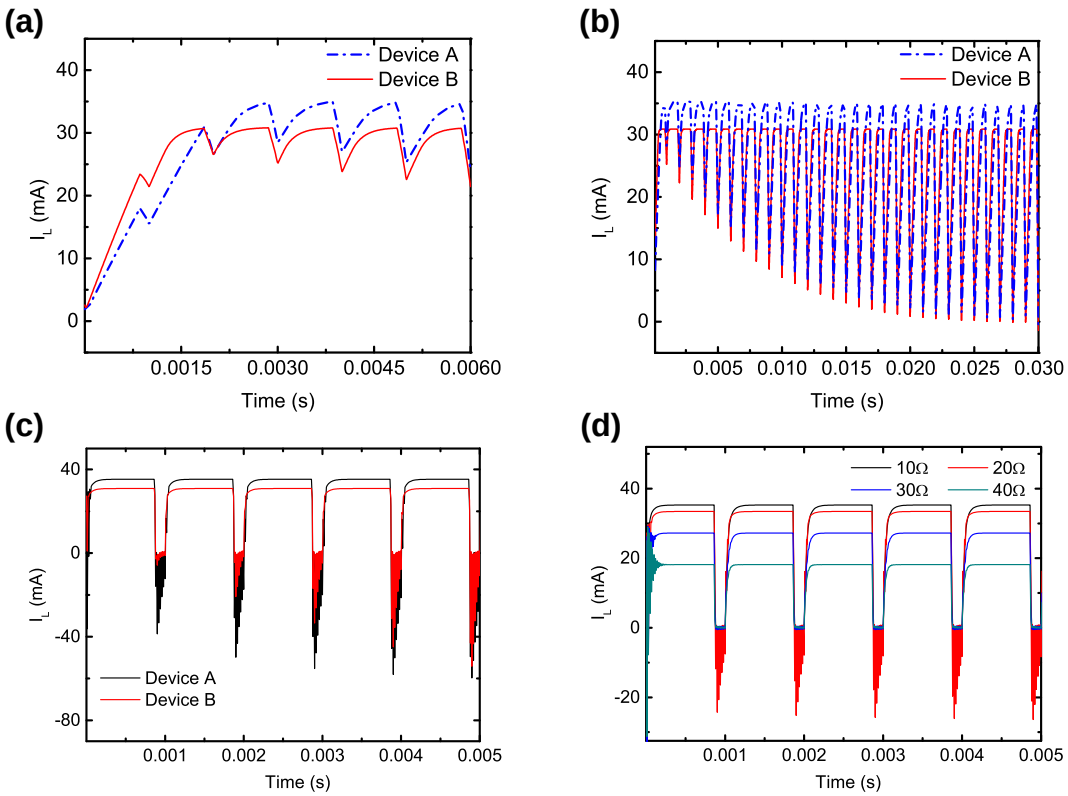

FIGURE 6 Transient response of the inductor current taking Devices A and B as the input source of (a) continuous conduction mode and (b) discontinuous conduction mode operated conventional boost converters; transient response of inductor current of the self-driven oscillator-based converter (c) taking Devices A and B as input source and (d) while varying the characteristic resistance of the input photovoltaic source from 10 to 40 Ω

lower J_{sc} and higher characteristics resistance ultimately results in a lower efficiency of the self-driven converter, as well as of the DCM operated conventional boost converter. Therefore, the results of this work suggest that while designing the indoor PV devices employing CZTSSe as the absorber layer, type-I band alignment should be preferred over type-II band alignment, if the PV device is to be used as an input to a Meissner oscillator-based self-driven up-converter, or DCM operated boost converter for efficiently driving low-power electronic loads. Though the study presented here is based on PV devices of a specific thin-film material, the theoretical framework employed here can be extended to the PV devices of other material systems so that their figure of merits can be correlated to performance characteristics of DC-to-DC converters designed for driving low-power electronic components of IoTs and cyber–physical systems.

4 | CONCLUSION

In summary, performance characteristics of self-driven DC-to-DC up-converters are evaluated taking as input CZTSSe-based indoor-PV devices such that the overall assembly of PV device and converter can be utilized to drive low-power components of cyber-physical systems under indoor illumination conditions. Output characteristics of the PV devices having different band alignments are first evaluated employing a device physics-based numerical model. Conversion efficiency and output voltage of the converter circuit have been subsequently correlated with the short-circuit current density and open circuit voltage of these devices. Results of the analysis suggest that the efficiency of the converter can in fact be higher for a PV device of lower efficiency, provided its short-circuit current density is sufficiently high. Similar dependence is obtained for conventional boost converters operating in a discontinuous conduction mode, whereas a continuous conduction mode of operation results in the opposite characteristic trend. Transient analysis shows that the higher short-circuit current density of the PV device results in a lower negative current through the inductive path of the converter circuit, thereby enhancing overall efficiency of the converter. The observed correlation between the operation of the indoor PV device and DC-to-DC up-converters emphasize the need for the device and circuit co-design such that desired output characteristics can be attained while driving low-power components of IoTs and cyber–physical systems.

ACKNOWLEDGMENT

This research received no specific grant from any funding agency in the public, commercial, or not-for-profit sectors

ORCID

Khandaker A. Haque https://orcid.org/0000-0002-0111-1568

Md Zunaid Baten https://orcid.org/0000-0003-0656-2728

REFERENCES

1. Tzounis, A., et al.: Internet of things in agriculture, recent advances and future challenges. Biosyst. Eng. 164, 31–48 (2017)
2. Lee J., Bagheri B., Kao H.A.: A cyber-physical systems architecture for industry 4.0-based manufacturing systems. Manuf. Lett. 3, 18–23 (2015)
3. Nasiri, A., Zabalawi, S.A., Mandic, G.: Indoor power harvesting using photovoltaic cells for low-power applications. IEEE Trans. Ind. Electron. 56(11), 4502–4509 (2009)
4. Carmo, J.P., Gonçalves, L.M., Correia, J.H.: Thermoelectric microconverter for energy harvesting systems. IEEE Trans. Ind. Electron. 57(3), 861–867 (2009)
5. Fang, H.B., et al.: Fabrication and performance of MEMS-based piezoelectric power generator for vibration energy harvesting. Microelectron. J. 37(11), 1280–1284 (2006)
6. Knight, C., Davidson, J., Behrens, S.: Energy options for wireless sensor nodes. Sensors. 8, 8037–8066 (2008)
7. Chong, Y.W., et al.: Energy harvesting for wearable devices: a review. IEEE Sensor J. 19, 9047–9062 (2019)
8. Paradiso, J.A., Starner, T.: Energy scavenging for mobile and wireless electronics. IEEE Pervasive Comput. 4(1), 18–27 (2005)
9. Freunek, M., Freunek, M., Reindl, L.M.: Maximum efficiencies of indoor photovoltaic devices. IEEE J. Photovolt. 3(1), 59–64 (2012)
10. Saha, A., Haque, K., Baten, M.Z.: Performance evaluation of single-junction indoor photovoltaic devices for different absorber bandgaps under spectrally varying white light-emitting diodes. IEEE J. Photovolt. 10, 539–545 (2019)
11. Minnaert, B., Veelaert, P.: Efficiency simulations of thin film chalcogenide photovoltaic cells for different indoor lighting conditions. Thin Solid Films. 519(21), 7537–7540 (2011)
12. Teran, A.S., et al.: AlGaAs photovoltaics for indoor energy harvesting in mm-scale wireless sensor nodes. IEEE Trans. Electron. Devac. 62(7), 2170–2175 (2015)
13. Mathews, I., et al.: Performance of III–V solar cells as indoor light energy harvesters. IEEE J. Photovolt. 6(1), 230–235 (2015)
14. Shen, K., et al.: CdTe solar cell performance under low-intensity light irradiance. Sol. Energy Mater. Solar Cell. 144, 472–480 (2016)
15. Lucarelli, G., et al.: Efficient light harvesting from flexible perovskite solar cells under indoor white light-emitting diode illumination. Nano Res. 10(6), 2130–2145 (2017)
16. Cho, S., et al.: Device and circuit codesign strategy for application to low-noise amplifier based on silicon nanowire metal–oxide–semiconductor field effect transistors. Jpn. J. Appl. Phys. 49(4S), 04DN03 (2010)
17. Swain, P.S., et al.: Device–circuit co-design for beyond 1 ghz 5 v level shifter using demos transistors. IEEE Trans. Electron. Dev. 60(11), 3827–3834 (2013)
18. Wang, W., et al.: Integration and Co-Design of Memristive Devices and Algorithms for Artificial Intelligence, pp. 101809. Elsevier Inc., Netherlands (2020). https://doi.org/10.1016/j.isci.2020.101809
19. Vaddi, R., et al.: Design and analysis of double-gate mosfets for ultra-low power radio frequency identification (rfid): device and circuit co-design. J. Low Power Electron. Appl. J. 1(2), 277–302 (2011)
20. Haque, K., Baten, M.Z.: On the prospect of CZTSSe-based thin film solar cells for indoor photovoltaic applications: a simulation study. AIP Adv. 9(5), 055326 (2019)
21. Yang, X., Xu, C., Giles, N.: Intrinsic electron mobilities in CdSe, CdS, ZnO, and ZnS and their use in analysis of temperature-dependent hall measurements. J. Appl. Phys. 104(7), 073727 (2008)
22. Simya, O., Mahaboobbatcha, A., Balachander, K.: A comparative study on the performance of kesterite based thin film solar cells using SCAPS simulation program. Superlattice Microst. 82, 248–261 (2015)
23. Scheer, R.: Towards an electronic model for $CuIn_{1-x}Ga_xSe_2$ solar cells. Thin Solid Films. 519(21), 7472–7475 (2011)
24. Redinger, A. et al.: Influence of S/Se ratio on series resistance and on dominant recombination pathway in $Cu_2ZnSn(SSe)_4$ thin film solar cells. Thin Solid Films. 535, 291–295 (2013)
25. Jacobi, K., Zwicker, G., Gutmann, A.: Work function, electron affinity and band bending of zinc oxide surfaces. Surf. Sci. 141(1), 109–125 (1984).
26. Islam, R., Nazif, K.N., Saraswat, K.C.: Si heterojunction solar cells: a simulation study of the design issues. IEEE Trans. Electron. Dev. 63(12), 4788–4795 (2016)
27. Gokmen, T., Gunawan, O., Mitzi, D.B.: Semi-empirical device model for $Cu_2ZnSn(S,Se)_4$ solar cells. Appl. Phys. Lett. 105(3), 033903 (2014)
28. Xu, J., Lin, J., Zhuang, C.: Analysis of the open-circuit voltage of $Cu_2ZnSn(S,Se)_4$ thin film solar cell. Sol. Energy. 164, 231–242 (2018)
29. Courel, M., et al.: Open-circuit voltage enhancement in CdS/Cu_2ZnSnS_4-based thin film solar cells: a metal–insulator–semiconductor (MIS) performance. Sol Energy Mater. Sol. Cell. 149, 204–212 (2016)
30. Robertson, J., Falabretti, B.: Electronic structure of transparent conducting oxides. In: D.S. Ginley, H. Hosono, D.C. Paine (eds.) Handbook of Transparent Conductors, pp. 27–50. Springer, Boston (2011). https://doi.org/10.1007/978-1-4419-1638-9_2
31. Robertson, J., Clark, S.: Limits to doping in oxides. Phys. Rev. B. 83(7), 075205 (2011)
32. Wang, W., et al.: Device characteristics of CZTSSe thin-film solar cells with 12.6% efficiency. Adv. Energy Mater. 4(7), 1301465 (2014)
33. Kirner, S., et al.: The influence of ITO dopant density on JV characteristics of silicon heterojunction solar cells: experiments and simulations. Energy Procedia. 77, 725–732 (2015)
34. Gloeckler, M., Fahrenbruch, A., Sites, J.: Numerical modeling of CIGS and CdTe solar cells: setting the baseline. In: Proceedings of 3rd World Conference on Photovoltaic Energy Conversion, 2003, 1, pp. 491–494. IEEE, Osaka (2003). https://ieeexplore.ieee.org/document/1305328
35. Sze, S.M., Ng, K.K.: Physics of Semiconductor Devices. John Wiley & Sons, Hoboken (2006). https://doi.org/10.1002/0470068329
36. Spies, P., Pollak, M., Mateu, L.: Handbook of Energy Harvesting Power Supplies and Applications. CRC Press, Boca Raton (2015). https://doi.org/10.1109/MIE.2016.2554721
37. Damaschke, J.M.: Design of a low-input-voltage converter for thermoelectric generator. IEEE Trans. Ind. Appl. 33(5), 1203–1207 (1997)
38. Pollak, M., Mateu, L., Spies, P.: Step-up DC-DC-Converter with coupled inductors for low input voltages. Fraunhofer IIS. 86, 625–632 (2008)
39. Hart, D.W.: Power Electronics. Tata McGraw-Hill Education, New York (2011)
40. Mohan, N.: Power Electronics: A First Course. Wiley, Hoboken (2011)

How to cite this article: Haque KA, Baten MZ. Correlation between performance characteristics of indoor photovoltaic devices and DC-to-DC up-converters for low-power electronic applications. *IET Circuits Devices Syst*. 2021;1–10. https://doi.org/10.1049/cds2.12069